Applied Physics A (2022) 128: 806
https://doi.org/10.1007/s00339-022-05885-3

Applied Physics A
Materials Science & Processing

Insight into dislocation activity during ECAP processing of AISI 304 stainless steel studied by X-ray diffraction profile analysis

K. Hajizadeh[1] · V. Abbasi-Chianeh[1] · K. J. Kurzydlowski[2]

Received: 17 May 2022 / Accepted: 19 July 2022 / Published online: 22 August 2022

Abstract

Despite many advantages of austenitic stainless steels, such as excellent formability, good corrosion resistance, and acceptable weldability, they suffer from low yield strength (YS). Grain refinement using equal channel angular pressing (ECAP) has been preferred as a promising method to strengthen these alloys. Due to the important role of dislocations both in the stage of microstructure refinement during deformation process and their subsequent work hardening effect in the final processed material, it is necessary to obtain information on the dislocation content of the material as well as the character and fraction of dislocations. The topic has been studied extensively on the stainless steels after deformation by conventional processes such cold rolling. However, a systematic study presenting sufficient detail after processing by severe plastic deformation methods such as ECAP is missing. For the first time, X-ray diffraction peak profiles have been analyzed for a severely deformed (by ECAP at 350 °C up to eight passes) AISI 304 austenitic stainless steel by this research. The modified Williamson–Hall and Warren–Averbach approaches were used to this end. Crystallite sizes obtained using these two methods are in a good agreement indicating that processing by eight passes ECAP refines the coherently scattering domain size down to nanometer range (average size $D = 68$ nm). Dislocation density (ρ) was found to increase during the initial stages of deformation and then to decrease after reaching a maximum. After that, it shows an upward trend again up to eight passes and approaches value of 4.71×10^{15} m^{-2}. The population of screw dislocations decreases gradually by applying ECAP deformation. A relatively equal fractions of both types of dislocations are present in the ECAP-ed material between equivalent strain of 2.8 and 4.8. With more deformation, screw dislocations in the structure increases again and reaches 74% after eight passes. At the same time, the effective outer cutoff radius of dislocations (Re) after a decrease during initial passes levels off to a saturated value around 80 nm, with continued deformation. Deformation-induced martensite (DIM) transformation does not occur during ECAP. This behavior was explained by a combination of high pressing temperature and greater stability of austenite phase in the studied material. Scanning transmission electron microscopy (STEM) observations of the microstructure showed a good correspondence with XRD data.

Keywords ECAP · AISI 304 · Dislocation density · Williamson–Hall method · Warren–Averbach method

1 Introduction

During the last two decades, numerous studies [1–6] confirmed that the initial coarse grain structure of austenitic stainless steels (ASSs) could be dramatically refined down to ultrafine (< 1 μm) and or nanocrystalline range (< 100 nm) by applying severe plastic deformation (SPD). It is known that, along with deformation twining and martensitic transformation, dislocation-controlled mechanisms play a key role in grain size refinement of these alloys when they are subjected to intense plastic deformation [1–6]. Accordingly, quantitative analysis such as determination of dislocation density, type of dislocations, subgrains size and distribution in combination with qualitative microstructural observations could aim to our better understanding about relationship between processing parameters and the obtained microstructural features [7–10].

Despite much activity in SPD processing of austenitic stainless steels, the literature reviews revealed that in most

---

✉ V. Abbasi-Chianeh
Vahid61abbasi@gmail.com

[1] Department of Materials Engineering, Urmia University of Technology, P.O.Box 57155-419, Urmia, Iran

[2] Faculty of Mechanical Engineering, Bialystok University of Technology, Bialystok, Poland

previous studies [1–6, 11] microstructure evolution and grain refinement was studied by methods of transmission electron microscopy (TEM) [1–6, 11] or by electron backscattering diffraction (EBSD) [2, 11]. TEM enables a direct observation of the microstructure and provides also information about the misorientation between adjacent grains/subgrains. However, it reveals information for a small fraction of the specimens investigated [12, 13]. In contrast, EBSD allows for obtaining grain size, texture, grain boundary character, etc., for a much larger area of samples [14]. On the other hand, preparation of representative samples for EBSD is challenging in terms of the flatness and polishing stresses.

Nowadays, XRD peak profile analysis emerged as a powerful tool for characterization of microstructure of metals [15]. It is frequently employed for determination of crystallite size and dislocation density/type in severely deformed metals [16–25]. Samples for XRD are simple to prepare and provide information for large areas of specimens [12, 13]. XRD peaks for plastically deformed metals are broadened [24] due to a small crystallite size and lattice microstrain within the diffracting domains [25]. In order to de-convolute these two effects, Warren–Averbach method [26] and Williamson-Hall analysis [24] are the two most commonly used procedures. In the present study we report the application of these two methods to XRD peak profile analysis of AISI 304 refined by ECAP process.

2 Experimental procedure

2.1 Materials and experiments

The material used in this investigation was a hot rolled commercial AISI 304 type austenitic stainless steel with a chemical composition given in Table 1. Material supplied in the form of rods was annealed at 1150 °C for one hour and then water-quenched to obtain an equiaxed microstructure with an average grain size of about 45 µm (Fig. 1). Rod-like samples 70 mm in length and diameter of 14.5 mm were machined and subjected to ECAP in a die with channels intersecting at an angle of $\Phi = 105^\circ$ and outer angle of $\Psi \approx 20^\circ$. This geometry yields an effective strain of about 0.8 per pass [20, 21]. ECAP was performed up to 8 passes at 350 °C at a constant ram speed of 1 mm/s using route BC whereby the billet was rotated by 90° counter clockwise between subsequent passes. A lubricant containing about 50% graphite powder, 25% MoS2 and 25% grease was used to reduce the friction.

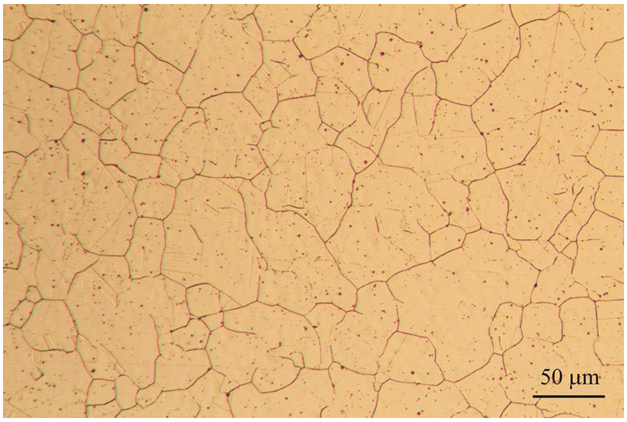

Fig. 1 Optical micrograph of AISI 304 stainless steel in the as-annealed condition

Microstructures of the as-pressed samples were observed by scanning transmission electron microscope (Hitachi HD 2700, operating at 200 kV). Specimens for STEM observations were cut from middle sections of the pressed billets parallel to the pressing direction. Thin foils for STEM were first mechanically ground to about 40 µm and finally electropolished in a Tenupol 5 double jet polishing unit in a solution of 10 vol % perchloric acid and ethanol at room temperature.

X-ray diffraction analysis was used to investigate the microstructural evolution of samples during ECAP. XRD patterns were recorded on a Bruker AXS D8-ADVANCE diffractometer using Cu Kα radiation of 0.15406 nm wavelength, 40 kV and 50 mA. Patterns were collected over the 2θ range of 40°–100° with a step size of 0.005° per step and a dwell time of 2 s per increment. A well-annealed coarse grain sample was used to make the correction on instrument specific broadening. Crystallite size, dislocation density, and fraction of different types of dislocations were determined as a function of number of ECAP passes by XRD peak profile analysis in

Table 1 Chemical composition of AISI 304 stainless steel utilized in the present study

Fe	N	Cu	P	S	Mo	Ni	Cr	Si	Mn	C
Balance	0.074	0.71	0.029	0.008	0.30	9.36	19.9	0.53	0.87	0.047

accordance with the modified Williamson–Hall and modified Warren–Averbach procedures.

2.2 The modified Williamson–Hall procedure

In the classical Williamson–Hall (WH) approach, the value of full width at half maximum (FWHM) for each single peak is obtained. Next, the following Williamson–Hall (WH) equation is constructed by plotting $\Delta K = (\mathrm{FWHM})\cos\theta/\lambda$ against $K = 2\sin(\theta)/\lambda$.

$$\Delta K = \left(\frac{0.9}{D}\right) + \varepsilon K \tag{1}$$

Here K is the length of scattering vector, λ is the wavelength of the incident beam, θ is the Bragg angle. D and ε represent the crystallite size and lattice microstrain, respectively [23]. A linear fit to the measured data is performed to extract the crystallite size and the lattice microstrain. The crystallite size is estimated from the intercept and the value of mean square lattice strain extracted from the slope of the linear extrapolation. Assuming that strain broadening is strictly caused by dislocations, Ungár [29] developed a unique methodology using the average contrast factor $\overline{C}$, called the modified Williamson–Hall (mWH) method and determined ΔK as follows:

$$\Delta K = \frac{0.9}{D} + \left(\frac{\pi M^2 b^2}{2}\right)^{\frac{1}{2}} \rho^{\frac{1}{2}} \left(K\overline{C}^{\frac{1}{2}}\right) + O\left(K\overline{C}^{\frac{1}{2}}\right)^2 \tag{2}$$

Crystallite size (D) can be obtained by plotting ΔK versus $K\overline{C}^{\frac{1}{2}}$ and extrapolating y-intercepts of the resulting graph. The effect of elastic anisotropy in each {hkl} crystal plane which leads to deviation from linear relation between ΔK versus K in WH plots is corrected by the average contrast factor, $\overline{C}$. The average contrast factor of dislocations which depends on the relative orientations between the Burgers vector, line vector of a dislocation, and the diffraction vector is described for cubic polycrystals as:

$$\overline{C}_{\mathrm{hkl}} = \overline{C}_{\mathrm{h00}}\left(1 - q\Gamma^2\right) \tag{3}$$

where Γ is the orientation parameter expressed by the following equation for a given crystal plane {hkl }:

$$\Gamma = \frac{\left(h^2k^2 + h^2l^2 + k^2l^2\right)}{\left(h^2 + k^2 + l^2\right)^2} \quad 0 \le \Gamma \le \frac{1}{3} \tag{4}$$

$\overline{C}_{\mathrm{h00}}$ is the average dislocation contrast factor in the crystal plane {h00}, and q is a parameter which depends on the dislocation type and elastic constants of the material. $\overline{C}_{\mathrm{h00}}$ and theoretical values of q can be determined numerically for two types of dislocations (screw/edge) in different slip system using the following equations [29]:

$$\overline{C}_{\mathrm{h00}} = \left(1 - f_{\mathrm{screw}}\right)\overline{C}^{\mathrm{edge}}_{\mathrm{h00}} + f_{\mathrm{screw}}\overline{C}^{\mathrm{screw}}_{\mathrm{h00}} \tag{5}$$

$$q = \left(1 - f_{\mathrm{screw}}\right)q^{\mathrm{edge}}_{\mathrm{th}} + f_{\mathrm{screw}}q^{\mathrm{screw}}_{\mathrm{th}} \tag{6}$$

where f_{screw} indicates the fraction of screw dislocations, $q^{\mathrm{screw}}_{\mathrm{th}}$ and $q^{\mathrm{edge}}_{\mathrm{th}}$ are values of q for the pure screw and pure edge dislocations calculated using Eq. 3. The influence of dislocations on diffraction peak broadening are included in the mWH approach (Eqs. 2) as dislocation density (ρ) and Burgers vector b. M and O are constants whose values depend on the dislocation's outer cutoff radius. Inserting Eq. 3 into Eq. 2 and neglecting the higher-order terms yields:

$$\frac{\Delta K^2 - \alpha}{K^2} \cong \frac{\pi M^2 b^2}{2}\rho\overline{C}_{\mathrm{h00}}\left(1 - q_{\mathrm{exp}}\Gamma\right) \tag{7}$$

where $\alpha = \left(\frac{0.9}{D}\right)^2$ and it must be estimated in such a way that a linear relationship with the minimum error value is established between the left-hand side of Eq. 7 and Γ. The experimental value of parameter $q(q_{\mathrm{exp}})$ can be extracted from the x-intercept of the regression line. From the experimentally obtained value of q, the fraction of screw dislocations can be determined. In order to determine the dislocation density, a further XRD peak profile analysis by using the modified Warren–Averbach (mWA) method needed.

2.3 The modified Warren–Averbach procedure

In mWA method the real part of the Fourier coefficients of diffraction peak profiles is written as a multiplication of the Fourier coefficients corresponding to the size and distortion effects [21]:

$$LnA_{\mathrm{L}} = Ln\left(A^{\mathrm{S}}_{\mathrm{L}}.A^{\mathrm{D}}_{\mathrm{L}}\right) = LnA^{\mathrm{S}}_{\mathrm{L}} - 2\pi^2L^2K^2 < \varepsilon^2_{\mathrm{K}} > \tag{8}$$

where A_{L}, $A^{\mathrm{S}}_{\mathrm{L}}$, $A^{\mathrm{D}}_{\mathrm{L}}$, and L indicate the real part of the Fourier coefficient, size Fourier coefficient, distortion Fourier coefficients, and Fourier variable, respectively. $< \varepsilon^2_K >$ is the mean square lattice strain arising from dislocations which can be written in terms of dislocation density and strain anisotropy as [30]:

$$< \varepsilon^2_{\mathrm{K}} > = \frac{\rho\overline{C}b^2}{4\pi}f(\eta) \tag{9}$$

where ρ and b indicate dislocation density and the magnitude of the Burgers vector respectively. $f(\eta)$ is the Wilkens function and η defined as $\eta = \mathrm{L}/\mathrm{R}_{\mathrm{e}}$ where R_{e} is the effective outer cutoff radius of dislocations. Inserting Eq. (9) into Eq. (8) yields the modified Warren–Averbach equation as [29]:

$$LnA_{\mathrm{L}} = LnA_{\mathrm{L}}^{\mathrm{S}} - \left(\frac{\pi b^2}{2}\right)\rho L^2 Ln\left(\frac{R_e}{L}\right)\left(K^2\overline{C}\right) + O(K^2\overline{C})^2 \tag{10}$$

where O represents the second-order term in $K^2\overline{C}$ and is small. By fitting LnA_L versus $K^2\overline{C}$, the slope $M(L) = \left(\frac{\pi b^2}{2}\right)\rho L^2 Ln\left(\frac{R_e}{L}\right)$ as the coefficient of the first-order term can be obtained for different value of L. Then dividing $M(L)$ by L^2 leads to the following equation:

$$\frac{M(L)}{L^2} = \frac{\pi b^2 \rho}{2} LnR_{\mathrm{e}} - \frac{\pi b^2 \rho}{2} LnL \tag{11}$$

The dislocation density and effective outer cutoff radius of dislocation can be determined by a linear fitting the left-hand side of Eq. 11 as function of ln(L). Size Fourier coefficient (A_L^S) for different values of L can be extracted from the y-intercept of the modified Warren–Averbach equation (Eq. 10).

3 Results and discussions

Figure 2a shows the XRD patterns of AISI 304 stainless steel in as-annealed condition and those subjected to severe plastic deformation by ECAP for different number of passes. It is seen that the studied material is fully austenitic both before and after deformation. This is in contradiction to data reported in the literature on formation of deformation-induced martensite (DIM) in 304 stainless steel during ECAP [1, 3–5].

This could be attributed primarily to the higher ECAP temperature of 350 ◦C used here and room temperature used by other researchers [4, 5, 12]. Moreover, composition induced stability of austenite phase of 304 steel used in the present study as estimated by Nohara equation [31] is relatively high (Md30 = – 22°C). A low Md30 temperature implies high stability of austenite against formation of DIM.

The individual peak profiles associated with (111), (200), (220), (311), and (222) reflections for the as-annealed specimens and those subjected to 2 and 8 ECAP passes are presented in Fig. 2b to f. The peaks for other number of passes are not included in this figure to simplify graphical analysis. The data in these figures include experimentally measured (symbols) and theoretically fitted profiles (solid lines, obtained by average of Lorentzian and Gaussian functions). Fitting accuracy, defined as difference between measured and fitted values, is also plotted at the bottom of the figures. FWHM values extracted from the fitted Lorentzian and Gaussian functions and after removing the instrumental broadening are listed in Table 2.

It can be seen from Fig. 2(b-f) and data of Table 2 that obvious peak broadening has occurred with increase in number of ECAP passes. This observation which is well consistent with previous reports [22, 32, 33] could be explained by a combination of smaller crystallite size and higher density of crystallographic defects especially dislocations formed in the microstructure with more straining during next ECAP passes.

Similar to the findings of some earlier investigations on SPD of austenitic stainless steels [34, 35], it is seen also here that XRD peaks shifted to higher angles after ECAP indicating a reduction in interplanar spacing and lattice parameter of austenite phase in the deformed specimens. This could be due to the fact that ECAP process generated a considerable amounts of residual compressive stresses in the structure [36]. Finally, one can observe that ECAP processing increased the intensity of (200) and (222) peaks. This apparently came at the expense of intensity of other peaks such as (220) and (311). This indicates that the crystal orientation of grains/subgrains in the 304 steel specimen after ECAP has a relatively large difference with that of the annealed starting material. Figure 3a shows classical Williamson–Hall plots of ΔK = (FWHM)cosθ/λ versus K = 2sin(θ)/λ for the samples after being ECAP-ed for 2 and 8 passes. It can be seen that 8-passes of ECAP results in higher ΔK values for every individual diffraction peak in comparison with 2P ECAP-ed sample. As is clear from the low fitting index (r- squared) values the data points for both 2P and 8P samples are highly scattered away from the fitting lines. This behavior arises from the fact that the elastic properties of each individual crystal plane greatly differ with those of other planes [29, 37]. For the present 304 stainless steel by assuming the elastic constants of C11 = 209, C12 = 133 and C44 = 121 GPa, in accordance with [38], the Young modulus of each plane (Ehkl) could be calculated as E111 = 289, E200 = 105, E220 = 201, E311 = 150 and E222 = 289 GPa by using Eq. 13 presented in Ref. [39]. (111) and (222) crystal planes are parallel each other and as seen they possess the highest Young modulus values. This means that lattice deformation is hard to occur in < 111 > or < 222 > directions but easy

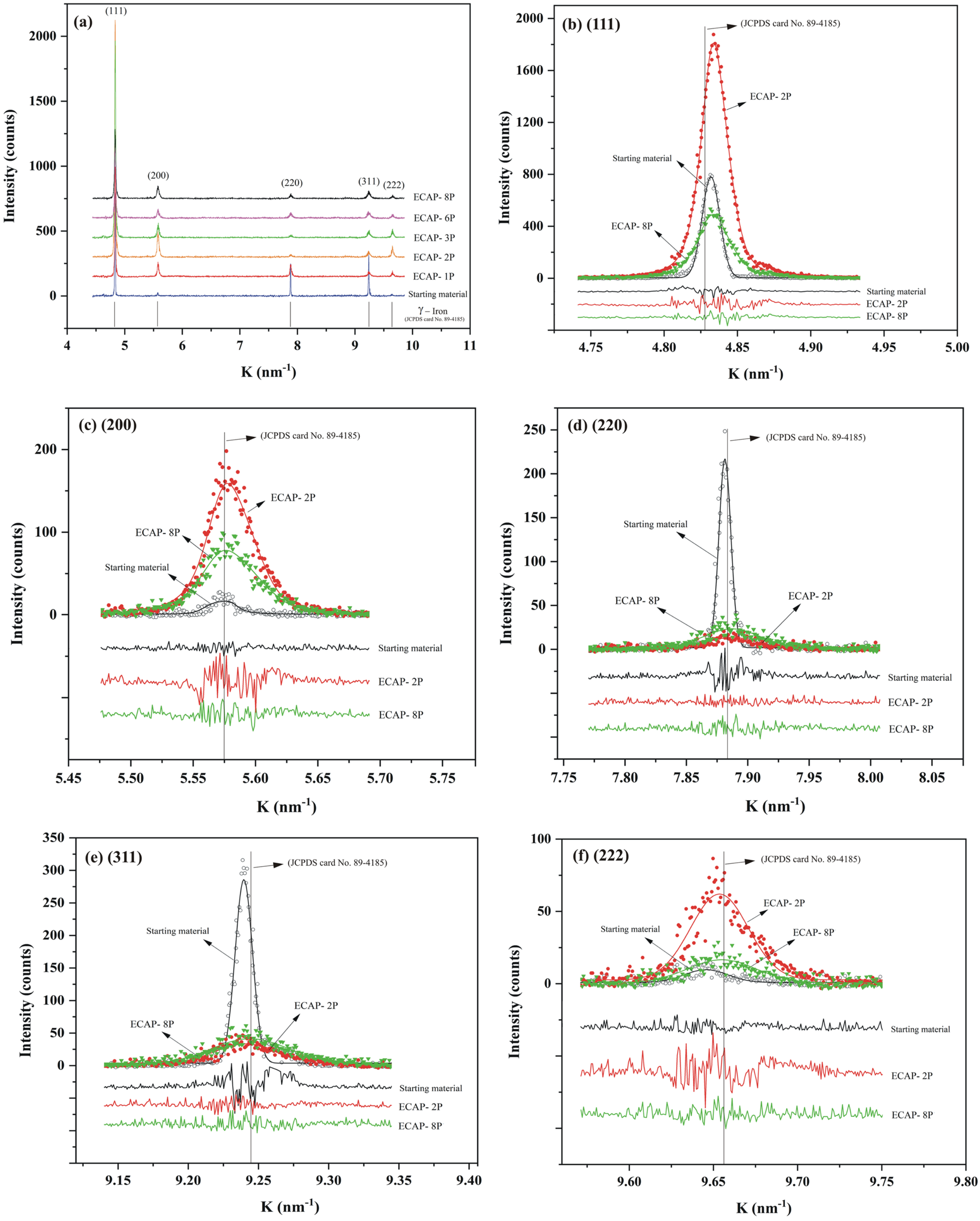

Fig. 2 **a** XRD patterns of AISI 304 stainless steel obtained from starting material as well as the samples subjected to ECAP for different number of passes where 1P, 2P …, 8P corresponds to the samples processed through 1, 2, …, and 8 passes, respectively, and **b-f** The individual peak profiles associated with (111), (200), (220), (311), and (222) reflections of the starting material and ECAP deformed specimens (2P and 8P)

Table 2 FWHM values of AISI 304 stainless steel obtained for starting material and ECAP-ed

(hkl)	Well annealed material		Starting material (0P)			1P			2P		
	Gauss	Lorentz	Gauss	Lorentz	*	Gauss	Lorentz	*	Gauss	Lorentz	*
(111)	0.013487	0.009933	0.014160	0.011750	0.003065	0.019404	0.016530	0.010271	0.022700	0.019270	0.013798
(200)	0.01703	0.014520	0.020910	0.018390	0.008001	0.038391	0.033641	0.026763	0.042452	0.037623	0.030992
(220)	0.008124	0.006934	0.011421	0.009450	0.005271	0.036290	0.031890	0.030162	0.045970	0.041141	0.039726
(311)	0.009201	0.0081210	0.014570	0.011982	0.007579	0.055133	0.052042	0.049138	0.055163	0.050764	0.048513
(222)	0.017202	0.014303	0.030301	0.022991	0.016817	0.038220	0.032730	0.026281	0.040361	0.036502	0.029356

(hkl)	3P			6P			8P		
	Gauss	Lorentz	*	Gauss	Lorentz	*	Gauss	Lorentz	*
(111)	0.023462	0.019950	0.014606	0.025800	0.022282	0.017171	0.02777	0.023731	0.019036
(200)	0.045330	0.041673	0.034580	0.046651	0.040783	0.034845	0.05036	0.045800	0.039337
(220)	0.059684	0.056191	0.054192	0.054820	0.049380	0.048330	0.0539	0.047773	0.047061
(311)	0.059081	0.055220	0.052729	0.066252	0.067091	0.062289	0.06476	0.062781	0.059381
(222)	0.044730	0.043165	0.035075	0.047120	0.046384	0.037974	0.04812	0.045504	0.038071

*FWHM magnitudes obtained after removing the instrument- related broadening: $FWHM* = \frac{1}{2}\left[\sqrt{FWHM^2_{Gauss(0-8P)} - FWHM^2_{Gauss(well\ annealed)}} + \left(FWHM_{Lorentz(0-8P)} - FWHM_{Lorentz(well\ annealed)}\right)\right]$

towards < 200 > or < 311 > . It is, therefore, expected that dislocations generated in (111) and (222) planes cause smaller elastically distorted region around themselves leading to less lattice elastic strain. The existence of lower magnitudes of inhomogeneous strain inside crystal lattice will make less peak broadening, and thus, low magnitudes are expected to be obtained for ΔK.

To construct the modified Williamson–Hall (mWH) plot with the aim of correcting the effect of elastic anisotropy in each {hkl} crystal plane, the contrast factor of dislocations was calculated using the ANIZC program. The program is available by access web browsers through the website http://metal.elte.hu/anizc. Regarding the crystal lattice of 304 stainless steel, the contrast factors were calculated for < 110 > (111) edge and screw dislocations as the most common dislocation type for metals with FCC lattice structure and the obtained results are listed in Table 3. Then, the orientation parameter Γ was calculated using Eq. 4 as 0.33 for (111), 0 for (200), 0.25 for (220), 0.16 for (311), and 0.33 for (222). The theoretical values of parameter q for screw and edge dislocations were determined on the assumption that there exists an equal fraction of both types of dislocations inside the metal. By plotting the values of contrast factor presented in Table 3 as a function of Γ, q_{th}^{screw} and $q_{\mathrm{th}}^{\mathrm{edge}}$ were obtained using Eq. 3 as 2.553 and 1.452, respectively. In order to estimate the experimental values of parameter q ($qexp$), the left-hand side of Eq. 7 plotted versus Γ as shown in Fig. 3b.

The best fitting lines obtained by considering the following values for α: 1.13×10^{-6}, 1.3×10^{-5}, 2.5×10^{-5}, 2.61×10^{-5}, 4.51×10^{-5}, and 1.7×10^{-4}, respectively, for the samples processed by ECAP for 0, 1, 2, 3, 6, and 8 passes. The points where regression lines crossed the x axis (x-intercept) gave the q_{exp} as: 2.49, 2.39, 2.22, 1.96, 1.99, and 2.26, respectively, for 0P, 1P, 2P, 3P, 6P, and 8P samples. Subsequently, we substituted q_{exp} values in Eq. 6 and parameter f_{screw} was determined as 0.94, 0.85, 0.7, 0.46, 0.49, and 0.73, respectively, for 0P to 8P samples. We substituted $fscrew$ values in Eq. 5 and the experimental contrast factor of dislocations in {h00} planes ($\overline{C}_{\mathrm{h00}}$ values) was determined as 0.2968, 0.2961, 0.2948, 0.2928, 0.2930, and 0.2951, respectively, for 0P to 8P samples. By placing the $\overline{C}_{\mathrm{h00}}$ and q_{exp} values obtained for each sample in Eq. 3, the contrast factor of dislocations in {hkl} planes ($\overline{C}_{\mathrm{hkl}}$ values) was determined for all samples and these data presented in Table 4. Finally, the modified Williamson–Hall (mWH) plots (Fig. 3c) were drawn by plotting ΔK versus $K\,\overline{C}^{\frac{1}{2}}$ and the crystallite sizes (D) were obtained by extrapolating y-intercepts of the resulting graphs. Compared to classical Williamson–Hall plots (Fig. 3a), although data points still show some scattering from regression lines, the magnitudes of fitting index display significant increase, thereby implying that the elastic anisotropy has been corrected reasonably by applying contrast factors, consistent with reports by Ungar [18, 25, 29].

Figure 4a shows the modified Warren–Averbach plots (Eq. 10) for the samples after being ECAP-ed for 2 and 8

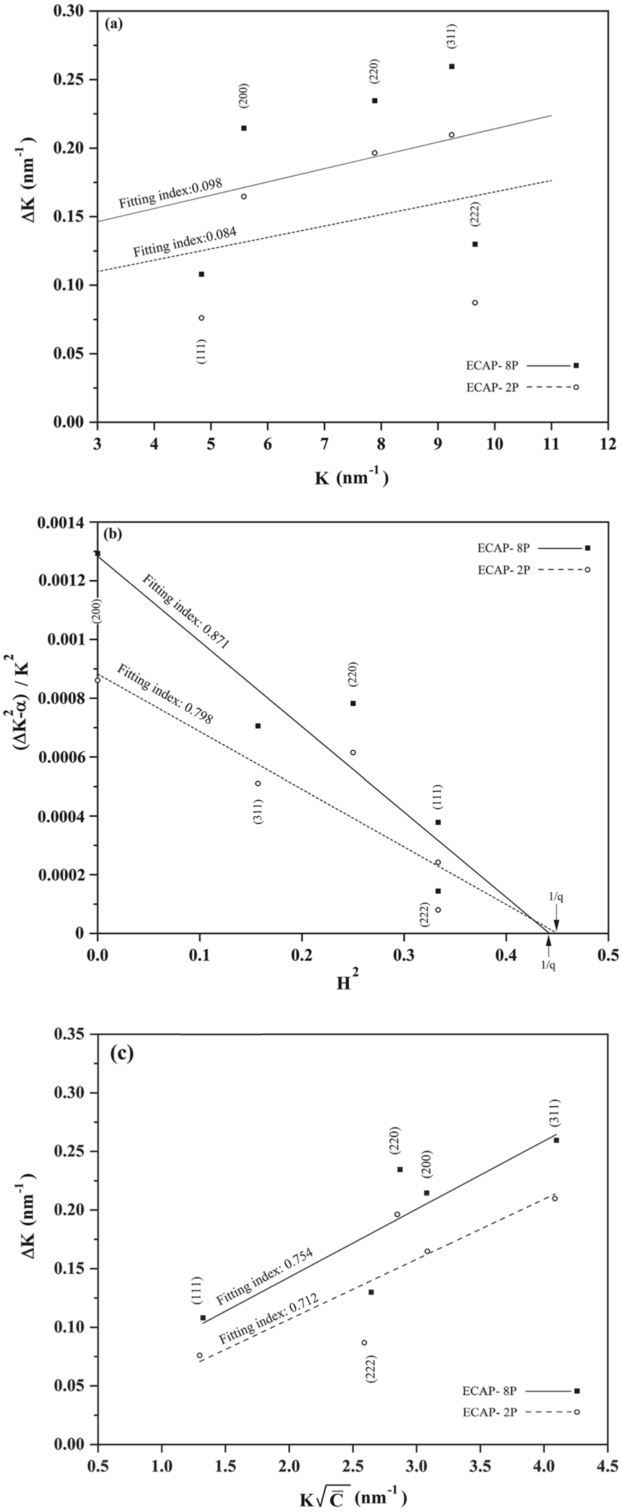

Fig. 3 Williamson–Hall procedure plots of AISI 304 stainless steel samples after ECAP processing for 2 and 8 passes: **a** classical Williamson–Hall plots, **b** plots of left-hand side of Eq. 7 versus orientation parameter, **c** modified Williamson-Hall plots

Table 3 Theoretical values of average contrast factor of dislocations ($\overline{c}_{\text{hkl}}^{\text{edge}}$ and $\overline{c}_{\text{hkl}}^{\text{screw}}$) calculated for different crystal planes of AISI 304 stainless steel

(hkl)	$\overline{c}_{hkl}^{edge}$	$\overline{c}_{hkl}^{screw}$
(111)	0.136536	0.0622668
(200)	0.288822	0.297406
(220)	0.174607	0.121052
(311)	0.217084	0.186638
(222)	0.136536	0.0622668

passes. These graphs were obtained by plotting *LnAL* versus $K^2\,\overline{C}$ for different selected magnitudes of Fourier length L. Size Fourier coefficient (A_{L}^{S}) for different values of L extracted after calculation of the *y*-intercepts for the fitted parabolic curves to data. After that, the A_{L}^{S} values were plotted as a function of Fourier length L (Fig. 4b) and x-intercept of tangent line to the resulting graphs at $L=0$ gave the apparent crystallite size (L0). In order to compute the dislocation density and effective outer cutoff radius of dislocations, the coefficient of the first-order term of the quadratic functions (M(L)) fitted to the data (Fig. 4a) was divided by L2 and the ratio of $\frac{M(L)}{L^2}$ was plotted against L (Fig. 4c). Dislocation density and effective outer cutoff radius of dislocations were obtained from the slope and *y*-intercept of regression lines, respectively. The results are summarized in Table 5.

The average crystallite sizes, *D* and L0, obtained by the modified Williamson–Hall and modified Warren–Averbach procedures, respectively, along with the dislocation density are plotted as a function of equivalent plastic strain imparted to the material by ECAP passes, and the results are shown in Fig. 5. Experimental values of parameter q (q_{exp}) and consequently the fraction of screw dislocations (*fscrew*) are plotted against strain in Fig. 6. From Table 5 and Fig. 5, it is found that the crystallite size rapidly decreases after the first pass ($\varepsilon_{\text{VM}}=0.8$), following which it shows a gradual decrease and reaches a minimum size of $D=68$ and $\text{L0}=78$ nm after eight passes ($\varepsilon_{\text{VM}}=6.4$). It is noted that although the rate of the increment is reduced with continued deformation, no saturation was attained in ECAP up to eight passes.

Also, though in the as-annealed starting material the crystallite size calculated from mWH approach exceeds remarkably that from mWA approach, after deformation both approaches match in satisfactory way. In terms of dislocation density, it is apparent from Fig. 5 that ρ initially increases continuously up to three passes ($\varepsilon_{\text{VM}}=2.8$) and reaches a maximum value of 6.15×10^{15} m^{-2}. After that it decreases and reaches 4.71×10^{15} m^{-2} after pass eight.

At the same time, experimental values of parameter q which range between $q_{\text{th}}^{\text{edge}}=1.45$ (pure edge) and $q_{\text{th}}^{\text{screw}}=2.55$ (pure screw) begin to decrease. The lowest values of q are calculated for $\varepsilon_{\text{VM}}=2.8$–4.8. After that q takes an

Table 4 Values of experimental contrast factor of dislocations in {hkl} planes ($\overline{C}_{hkl}$) obtained for AISI 304

(hkl)	0P	1P	2P	3P	6P	8P
(111)	0.050763	0.199565	0.20488	0.200007	0.2083	0.253652
(200)	0.2968	0.091895	0.087748	0.15582	0.128917	0.09713
(220)	0.112272	0.172648	0.175627	0.18896	0.188463	0.214521
(311)	0.180898	0.142616	0.142966	0.176635	0.166324	0.170863
(222)	0.050763	0.199565	0.20488	0.200007	0.2083	0.253652

Stainless steel samples after ECAP processing for different number of passes

upward trend up to eight passes. This indicates that early stages of ECAP processing gradually replace screw dislocations by edge dislocations. In the as-received material over 90% of dislocations are of screw type and equal fractions of both types of dislocations appear in the ECAP-ed material for equivalent strain of 2.8–4.8. However, further deformation increases population of screw dislocations in the structure up to 74% after eight passes.

The values of effective outer cutoff radius of dislocations (Re) obtained after different processing conditions are given in Table 5. It appears that a significant decrease in R_e occurred after a single pass of ECAP. With increasing ECAP passes to 3, R_e decreases again but with a more gradual increment. Additional deformation up to 8 passes caused no remarkable change and Re leveled off to a saturated value around 80 nm. The degree of distortion of lattice around a dislocation core depends on distance to between dislocations, i.e., on their density and arrangement [40]. Rearrangement of dislocations into low energy configurations such as low-angle grain boundaries or dipoles is a clear example in which there is a strong overlapping in the strain fields of dislocations [40]. Considering the above explanations, reduction in Re values after processing by ECAP gives an evidence that grain size refining in the present 304 steel is mainly resulting from dislocation generation, sliding and rearrangement. Dislocation cell walls generated during initial stage of deformation gradually evolve into low energy dislocation configurations and form sub-grain low-angle boundaries. Transformation of these boundaries into high-angle ones takes place after processing at high number of ECAP passes.

The results of XRD analysis agree with direct STEM observations of the microstructures of ECAP-ed specimens as illustrated by micrographs for 8 passes sample presented in Fig. 7. The images in Fig. 7 show the same region in bright (Fig. 7a) and dark field mode (Fig. 7b). Both micrographs show that an apparent refinement down to ultrafine/nanocrystalline range occurred by ECAP in the microstructure.

Extremely fine equiaxed grain/subgrains generally less than 100 nm in size are frequently observed (e.g., the grains indicated by red arrows in Fig. 7a and b. Also narrow and elongated grains could be found of the width lower than 70 nm—marked in a rectangle in Fig. 7b.

A careful examination of the contrast inside the grains both in the bright (Fig. 7a) and dark field (Fig. 7b) micrographs shows that most of the grain/subgrains contain high density of dislocations. However, grains nearly free of lattice dislocations are also present in the structure—marked by red circles in Fig. 7a and b. Such inhomogeneous structure is typical of SPD-processed metals and alloys, as discussed in Ref. [27, 29, 41].

Based on the data presented in Table 5, the size parameters obtained after ECAP for eight passes are $D = 68.3$ and $L0 = 78.3$ nm. These values, which can be interpreted as size of coherently scattering domains [18–22, 32, 33, 42], agree well with STEM observations carried out on the same specimens containing large number of nano-sized equiaxed grain/subgrains.

In grain size measurements of based on STEM images only crystals surrounded by sharp boundaries were taken into account. On the other hand, it can be seen in Fig. 7a and b that the contrasts within grains vary in the way which indicates dislocation cells with sizes of a few tens of nanometers exists in their interiors (regions marked as A in Fig. 7b). The smallest microstructural crystallite-like element in the STEM micrographs has size lower than 70 nm. As a consequence, one may conclude that there is a good agreement between the results of XRD analysis and direct observations of the microstructure by STEM.

4 Conclusion

X-ray peak profile analysis was applied to AISI 304 austenitic stainless steel after deformation by ECAP at 350°C for different number of passes. Evolution of crystallite size as well as

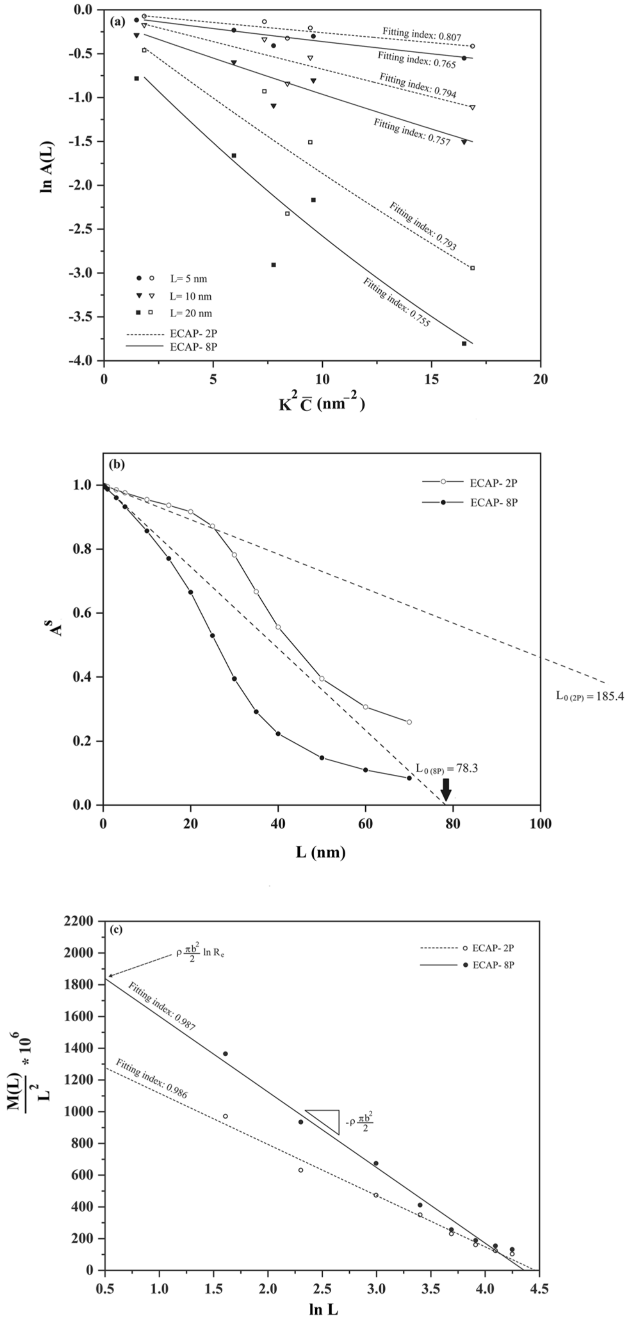

Fig. 4 Modified Warren–Averbach plots of AISI 304 stainless steel samples after ECAP processing for 2 and 8 passes: **a** plots of versus for different selected magnitudes of Fourier length L, **b** plots of values as a function of L, **c** Plots of against L

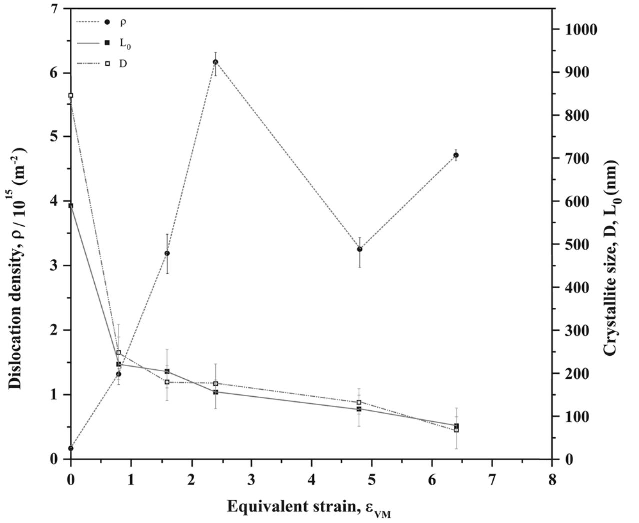

Fig. 5 Evolution of crystallite size (D, L0) and dislocation density (ρ) in AISI 304 stainless steel as a function of equivalent plastic strain imparted to the material during ECAP

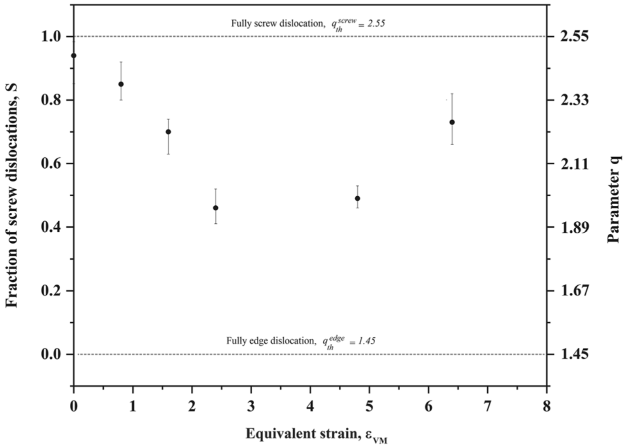

Fig. 6 Change in the fraction of screw dislocations and the value of parameter q with equivalent plastic strain in ECAP-ed AISI 304 stainless steel samples

changes in the dislocation density and dislocation character was evaluated quantitatively after consecutive ECAP passes. The obtained results lead to the following conclusions:

Table 5 Microstructure parameters obtained from the X-ray peak profile analysis of AISI 304

f_{screw} (%)	Re (nm)	ρ (×10^{15} m^{-2})	L_0 (nm)	*D* (nm)	Processing conditions
94	288	0.21	590	845	Starting material -0P
85	113	1.32	224	249	ECAP- 1P
70	87	3.19	204.9	180	ECAP- 2P
46	82	6.15	156.4	176	ECAP- 3P
49	83	3.27	118.7	134	ECAP- 6P
73	79	4.71	78.3	68.3	ECAP- 8P

Stainless steel after different processing conditions: (*D*) and (L_0) are the average crystallite size obtained by the modified Williamson–Hall and modified Warren–Averbach procedures, respectively. (ρ) denotes dislocation density, (R_e) is the effective outer cutoff radius of dislocations, and (f_{screw}) indicates the fraction of screw dislocations

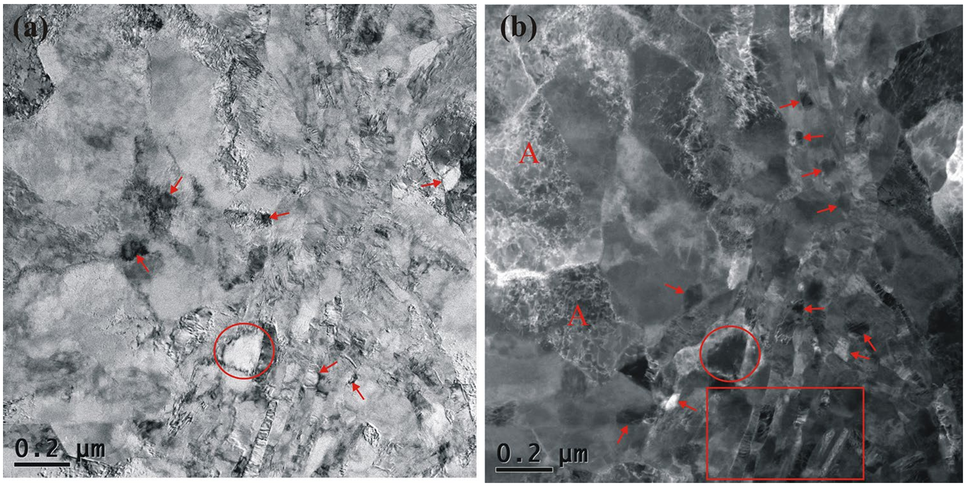

Fig. 7 **a** Bright field and **b** dark field STEM micrographs taken from the longitudinal section of a AISI 304 stainless steel sample after processing by 8 passes of ECAP at 350 °C

(1) Deformation-induced martensite (DIM) transformation does not occur during ECAP. This behavior was explained by a combination of relatively high pressing temperature and composition induced stability of austenite phase in the studied material.
(2) Crystallite size (*D*) as determined by X-ray diffraction changes from 249 to ~ 68 nm with increasing number of ECAP passes. These values are in a good correlation with the estimates based on STEM observations.
(3) The crystallite size values (*D*, L0) obtained using the modified Williamson–Hall and modified Warren–Averbach approaches are in good agreement with each other.
(4) Dislocation density in ECAP processed specimens increases up to three passes and reaches a maximum value of 6.15×10^{15} m^{-2}. For higher number of ECAP passes, it decreases down to 4.71×10^{15} m^{-2} after pass eight.
(5) Changes in the density of dislocations are accompanied by shift in their character with ECAP deformation. Approximately equal fractions of both types of dislocations are present in the ECAP-ed material between equivalent strain of 2.8 and 4.8. For total plastic deformation exceeding 4.8, density of screw dislocations increases and reaches 74% after eight passes.
(6) Effective outer cutoff radius of dislocations (Re) levels off to a saturated value around 80 nm, which is close to the average size crystallites.

Declarations

Conflict of interest The authors declare that there is no conflict of interest.

References

1. Z.J. Zheng, J.W. Liu, Y. Gao, Mater. Sci. Eng. A (2017). https://doi.org/10.1016/j.msea.2016.11.004
2. G.G. Yapici, I. Karaman, Z.P. Luo, H.J. Maier, Y.I. Chumlyakov, J. Mater. Res. (2004). https://doi.org/10.1557/JMR.2004.0289
3. Z.J. Zheng, Y. Gao, J.W. Liu, M. Zhu, Mater. Sci. Eng. A (2015). https://doi.org/10.1016/j.msea.2015.05.085
4. C.X. Huang, Y.L. Gao, G. Yang, S.D. Wu, G.Y. Li, S.X. Li, J. Mater. Res. (2006). https://doi.org/10.1557/jmr.2006.0214
5. C.X. Huang, G. Yang, B. Deng, S.D. Wu, S.X. Li, Z.F. Zhang, Phil. Mag. (2007). https://doi.org/10.1080/14786430701594046

6. K. Hajizadeh, K.J. Kurzydlowski, Phys. Met. Metallogr. (2021). https://doi.org/10.1134/S0031918X21300013
7. X.L. Shi, W.D. Liu, M. Li, Q. Sun, S.D. Xu, D. Du, J. Zou, Z.J. Chen, Adv. Energy. Mater. (2022). https://doi.org/10.1002/aenm.202200670
8. W.Y. Chen, X.L. Shi, J. Zou, Z.J. Chen, Small. Methods. (2022). https://doi.org/10.1002/smtd.202101235
9. Z.J. Chen, W.D. Liu, J Mater. Sci. Technol. (2022). https://doi.org/10.1016/j.jmst.2021.12.069
10. X.L. Shi, X. Tao, J. Zou, Z.J. Chen, Adv. Sci. (2020). https://doi.org/10.1002/advs.201902923
11. Y. Mine, K. Koga, K. Takashima, Z. Horita, Mater. Sci. Eng. A. (2016). https://doi.org/10.1016/j.msea.2016.03.018
12. T. Shintani, Y. Murata, Acta Mater. (2011). https://doi.org/10.1016/j.actamat.2011.03.055
13. R. Kishor, L. Sahu, K. Dutta, A.K. Mondal, Mater. Sci. Eng. A. (2014). https://doi.org/10.1016/j.msea.2014.01.043
14. F.J. Humphreys, Scr. Mater. (2004). https://doi.org/10.1016/j.scriptamat.2004.05.016
15. A. Bishnoi, S. Kumar, N. Joshi, Microsc. Method. Nanomater. Charact. (2017). https://doi.org/10.1016/B978-0-323-46141-2.00009-2
16. A. Grayeli-korpi, H. Savaloni, M. Habibi, Appl. Surf. Sci. (2013). https://doi.org/10.1016/j.apsusc.2013.03.081
17. S. Dey, N. Gayathri, P. Mukherjee, A. Dutta, M.K. Mitra, Philos. Mag. (2022). https://doi.org/10.1080/14786435.2021.1985735
18. T. Ungar, J. Gubicza, P. Hanak, I. Alexandrov, Mater. Sci. Eng. A (2001). https://doi.org/10.1016/S0921-5093(01)01025-5
19. E. Schafler, M. Zehetbauer, A. Borbely, T. Ungar, Mater. Sci. Eng. A. (1997). https://doi.org/10.1016/S0921-5093(97)00168-8
20. A. Borbely, J.H. Driver, T. Ungar, Acta Mater. (2000). https://doi.org/10.1016/S1359-6454(99)00457-7
21. I.C. Dragmoir, M. Gheorghe, N. Thadhani, R.L. Snyder, Mater. Sci. Eng. A. (2005). https://doi.org/10.1016/j.msea.2005.04.028
22. M. R. Movaghar Garabagh, S. Hossein Nedjad, H. Shirazi, M. Iranpour. Mobarekeh, M. Nili Ahmadabadi. (2008) Thin Solid Films. doi: https://doi.org/10.1016/j.tsf.2008.04.019
23. K.R.Desai, S.T.Alone, S.R.Wadgane, Sagar E.Shirsath, Khalid M.Batoo, A.Imran, E.H.Raslan, M.Hadi, M.F.Ijaz, R.H.Kadam, Physica B: Physics of Condensed Matter, (2021) https://doi.org/10.1016/j.physb.2021.413054
24. G.K. Williamson, W.H. Hall, Acta. metal. **1**, 22 (1953)
25. T. Ungar, J. Gubicza, G. Ribarik, A. Borbely, J. Appl, Cryst. (2001). https://doi.org/10.1107/S0021889801003715
26. B.E. Warren, B.L. Averbach, J. Appl. Phys. **21**, 595 (1950)
27. R.Z. Valiev, R.K. Islamgaliev, I.V. Alexandrov, Prog. Mater. Sci. (2000). https://doi.org/10.1016/S0079-6425(99)00007-9
28. R.Z. Valiev, T.G. Langdon, Prog. Mater. Sci. (2006). https://doi.org/10.1016/j.pmatsci.2006.02.003
29. T. Ungar, I. Dragomir, A. Revesz, A. Borbely, J. Appl, Cryst. (1999). https://doi.org/10.1107/S0021889899009334
30. M. Wilkens, Phys. Status. Solidi. A. **2**, 359 (1970)
31. K. Nohara, Y. Ono, N. Ohashi, Tetsu-to-Hagané **63**, 772 (1977)
32. J. Gubicza, L. Balogh, R.J. Hellmig, Y. Estrin, T. Ungar, Mater. Sci. Eng. A. (2005). https://doi.org/10.1016/j.msea.2005.03.042
33. J. Gubicza, N.H. Namb, L. Balogh, R.J. Hellmig, V.V. Stolyarov, Y. Estrin, T. Ungár, J. Alloy. Comp. (2004). https://doi.org/10.1016/j.jallcom.2003.11.162
34. H. Ueno, K. Kakihata, Y. Kaneko, S. Hashimoto, A. Vinogradov, J. Mater. Sci. (2011). https://doi.org/10.1007/s10853-011-5303-4
35. P. Zhang, W. Han, Z. Huang, G. Li, M. Zhang, J. Li, Mater. Res. Express (2011). https://doi.org/10.1088/2053-1591/ac1ecc
36. G. Németh, K. Horváth, C. Hervoches, P. Cejpek, J. Palán, M. Duchek, K. Máthis, Metals (2018). https://doi.org/10.3390/met8121000
37. S. Takaki, F. Jiang, T. Masumura, T. Tsuchiyama, ISIJ. Int. (2018). https://doi.org/10.2355/isijinternational.ISIJINT-2017-642
38. H.M. Ledbetter, Physica B+ C 128(1), 1 (1985)
39. M. Rabiei, A. Palevicius, A. Dashti, S. Nasiri, A. Monshi, A. Vilkauskas, G. Janusas, Materials (2020). https://doi.org/10.3390/ma13194380
40. D.E. Porter, K.E. Easterling, M.Y. Sherif, 3rd. Ed. (CRC Press, 2009), pp. 44- 51
41. K. Hajizadeh, S. Ejtemaei, B. Eghbali, Appl. Phys. A (2017). https://doi.org/10.1007/s00339-017-1123-y
42. M.S. Abd El-Sadek, H.S. Wasly, K. Mujasam Batoo, *Appl* (A, Phys, 2019). https://doi.org/10.1007/s00339-019-2576-y